WILEY | Hindawi

Research Article

Genetic Programming-Based Prediction Model for Microseismic Data

Man Wang,[1] Hongwei Zhou,[2] Dongming Zhang [ID],[3,4] Yingwei Wang,[1] Weihang Du,[3,4] and Beichen Yu[3,4]

[1]*State Key Laboratory of Coking Coal Exploitation and Comprehensive Utilization, China Pingmei Shenma Holding Group CO., LTD, Pingdingshan, Henan 467000, China*
[2]*School of Energy and Mining Engineering, China University of Mining and Technology (Beijing), Beijing 100083, China*
[3]*State Key Laboratory of Coal Mine Disaster Dynamics and Control, Chongqing University, Chongqing 400030, China*
[4]*School of Resources and Safety Engineering, Chongqing University, Chongqing 400030, China*

Correspondence should be addressed to Dongming Zhang; zhangdm@cqu.edu.cn

Microseismic monitoring is a rock breakdown monitoring technology, and it has become a major technical tool for underground disaster warning and prevention. However, the massive amount of data involved in multipoint monitoring raises the difficulty for microseismic research when the research object involves underground large-scale complex engineering on time and space scales. The risk predictions of rockburst based on microseismic parameters rely only on the experience of researchers and subjective factors by the human factor. The dependent variable cannot be related to the acoustic and energy signals in the form of a functional equation. Therefore, we collected a large amount of microseismic data obtained from the working faces of Shoushan Mine of Pingdingshan Coal Group in China and filtered the data, then we constructed a prediction model of microseismic data based on underground spatial three-dimensional coordinates using genetic programming (GP), which can realize real-time monitoring and disaster warning of microseismic signals. We established the magnitude and energy prediction formulas by GP and obtained the real-time evolution of each parameter of the optimal individual. The results showed that the actual seismic and energy data of the working faces exhibited good agreement with those predicted by the prediction formulas. The high energy and seismic distribution were caused by the mining stress at the edge of working faces due to the excavation and unloading effect of the surface, and the energy and seismic evolution predicted by GP could also show this phenomenon well.

1. Introduction

In the China's 14th Five-Year Plan, the science and technology development will focus on frontier areas, i.e., deep earth, deep sea, aviation, and space technology [1]. Deep underground space is rich in coal, oil, and unconventional natural gas resources, but it is also under complex geological condition of high in situ stress, fluid pressure, and temperature with strong mining disturbance [2–4]. Therefore, the energy extraction is highly susceptible to rock burst and other dynamic hazards, which become a challenge to the efficient development of deep earth resources [5–9].

Microseismic monitoring technology is a rock fracture monitoring technology and has become a major technical tool for early warning and prevention of subsurface hazards [10–12]. Based on the acoustic and energy signals transmitted by rock mass during breakdown, it analyzes the source characteristics and assesses the damage of rock mass, thus provides a theoretical basis for controlling rock dynamic hazards [13, 14]. Many scholars have evaluated the reservoir stability and production status based on microseismic monitoring [15–17]. Tang et al. [18] analyzed the distribution of rock burst in multipanel and multistope areas with simultaneous mining and designed sensor network spatial arrangement schemes with the optimized multiple microseismic monitoring systems. Maxwell et al. [19] monitored the deformation in Yibal oil field and other fields by identifying the microseismic signal characteristics and located the

microseismic sources accordingly. Tang et al. [20] analyzed the rockburst mechanism in tunnel by microseismic monitoring and pointed out that the rockburst was induced by the interaction between rock and surrounding rock and deformation localization. Zhang et al. [21] used a microseismic monitoring system to obtain microseismic energy during mining and defined new rockburst prediction parameters. They established the relationship between microseismic energy and rock damage to effectively assess the stability of coal and rock mass.

The acoustic and energy data obtained from microseismic monitoring provide an effective database for early warning and prevention and control of dynamic hazards. However, the large amount of data involved in multipoint monitoring raises the difficulty of microseismic research because the research objects generally involve the complex engineering on large temporal and spatial scales underground. Moreover, the risk prediction of rockburst based on microseismic parameters relies only on the experience of researchers and is greatly influenced by human subjective factors [22]. Therefore, using machine learning algorithm to process the microseismic data has become a research hotspot [23–25]. It can also ensure the accuracy and precision of the data. Wang et al. [26] proposed a self-optimization mechanism and introduced a machine learning algorithm called automatic detection network, which could monitor microseismic signals in real time. Tang et al. [27] proposed a new end-to-end training network architecture to automatically identify microseismic signals. The accuracy of intelligent microseismic monitoring was greatly improved by autonomously adjusting the weights of dependent variables without increasing the computational cost. Ma et al. [28] used a numerical method to simulate the progressive damage of coal seam floor during mining and constructed a microseismic monitoring system. They used virtual reality to realize 3D visualization of microseismic monitoring and analyzed the damage characteristics of the floor more accurately.

Current scholars have used machine learning for effective processing of microseismic data. However, most of the studies often require much time to find the optimal or near-optimal network structure for microseismic signal monitoring and tuning, and they cannot relate the dependent variable to the acoustic and energy signals in the form of a functional equation [29, 30]. Genetic programming (GP), as an extension of genetic algorithm (GA), provides a new soft computing approach to solve this method [31–33]. It does not require users to adjust the weights and can automatically evolve the type, structure, and parameter of the required model. It explicitly derives predictive equation to describe the relationship between variables. Effective prediction of GP in geomechanics has been demonstrated [34–36]. Therefore, we collected a large amount of microseismic data obtained from the working faces of Shoushan Mine of Pingdingshan Coal Group in China and filtered the data, then we constructed a prediction model of microseismic data based on underground spatial three-dimensional coordinates using GP. The prediction formulas for microseismic data were obtained, which can realize real-time monitoring and disaster warning of microseismic data.
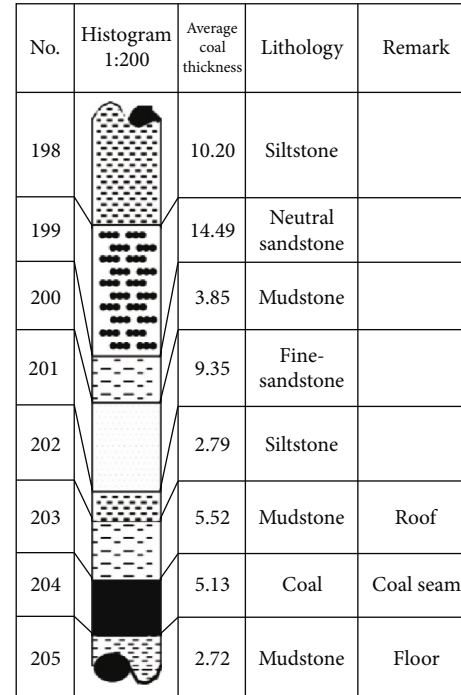

No.	Histogram 1:200	Average coal thickness	Lithology	Remark
198		10.20	Siltstone	
199		14.49	Neutral sandstone	
200		3.85	Mudstone	
201		9.35	Fine-sandstone	
202		2.79	Siltstone	
203		5.52	Mudstone	Roof
204		5.13	Coal	Coal seam
205		2.72	Mudstone	Floor

FIGURE 1: Comprehensive histogram of roof and floor slate of coal seam in 12070 working face.

2. Geological Information

In this study, the microseismic data were taken from the 12070 and 12090 working faces of Shoushan Mine of Pingdingshan Coal Group in China. Shoushan Mine is located in the northeast of Pingdingshan City, with a shaft field of 6.1 km long in east-west direction and 4.4 km wide in north-south inclination. The average depth of the coal seam in the well field is 750 m, with an inclination angle of 8°~12°. The coal seams H_{15} and H_{16-17} are both coal seams with outburst risk. The working face of 12070 is located in the east of Shoushan Mine's hexagonal mining area, with a strike length of 1 580 m and a design mining length of 240 m. The coal seam of H_{15-17} was mined with a mining height of 4.0 m. The comprehensive histogram of roof and floor slate of coal seam in 12070 working face is shown in Figure 1. The average burial depth of 12090 working face is 455 m, and the average coal thickness is 4.5 m. The surrounding rock is generally monoclinic structure with a slightly westward inclination to the north. The dip angle is around 10°. The original gas content is 4.32 m³/t, and the Protodyakonov coefficient of the coal seam is 0.17. The gas pressure was measured as 0.21 MPa. According to the available geological data, there is no obvious structure in this working face, but the top and bottom plates are undulating. It has a certain impact on the excavation. The lithology of roof and floor slate of coal seam in 12090 working face is shown in Table 1. In this study, 7851 microseismic data near 12070 and 12090 working faces are selected for this study, and their magnitude distribution is from 0.41 to 6.86. The depth distribution of microseismic data is from 0 to -1400 m. The rule of sensor recording data is that when

TABLE 1: Lithology of roof and floor slate of coal seam in 12090 working face.

Title		Rock	Thickness/m	Lithology
Roof	Main roof	Dazhan sandstone	3~12.1	Deep gray, gray black, quartz mainly argillaceous cementation thick layer; local microsandy mudstone.
	Immediate roof	Sandy mudstone	4~10.9; average 7.4	Deep gray, gray black, medium-thick stratiform mica flakes, and carbonaceous local sandy mudstones containing fossil plants.
	False roof	Mud or sandy mudstone	0.5~3; average 1.7	Soft, broken, and easy to fall.
Floor	Immediate floor	Mud or sandy mudstone	0~2.6	Black ash, black, thin-layer carbonaceous, and plant fossils, undulating. It may have an impact on recovery.
	Main floor	Sandy mudstone or fine sandstone	3.1~8.3	Gray black, gray, pyrite-bearing nodules and argillaceous bands visible in large quantities of pyrite nodules and siderite nodules.

any sensor received a signal exceeding the set threshold, the data from 500 ms before to 1000 ms after the reception of this signal was intercepted by all sensors as a microseismic data. The next step is to filter the energy and magnitude data obtained from the field microseismic data monitoring to exclude the interference of noise.

3. Filtering of Sample Data

The original microseismic waveform obtained from the sensor contained large background noise, so the original waveform needed to be filtered. Filtering is an operation that filters out specific wave frequencies (high or low-frequency) from the signal to extract the desired signal [37]. Generally, high-frequency signals in images are the points in the image that have significant grayscale changes and present contours or noise, while low-frequency signals show flat and insignificant grayscale changes in the image. According to the high and low frequencies of the image, corresponding high and low pass filters can be designed. High pass filtering detects sharp and obvious changes in the image, while low pass filtering makes the image smooth and filters out the noise in the image. The filter is often designed as a discrete-time system. So the system input is a time series of $x(t)$, and the output is $y(t)$. $y(t)$ versus $x(t)$ can be expressed as follows [38]:

$$y(t) = h(t) \otimes x(t) + n(t), \tag{1}$$

where $h(t)$ denotes the response between the input and output, $\otimes$ denotes the convolution sign, and $n(t)$ denotes the additive noise caused by the inverse filtering to achieve the best recovery of smoothing metric. $n(t)$ is not correlated with $x(t)$. Fourier transform of the above equation can be obtained:

$$Y(j\omega) = H(j\omega) \otimes X(j\omega) + N(j\omega), \tag{2}$$

where $H(j\omega)$ is the transfer function of the filter, which reflects the frequency characteristics of the filter. $N(j\omega)$ is the power spectrum of the additive noise.

Low pass filtering involves the linear mean filter, Gaussian filter, nonlinear bilateral filter, and median filter; high pass filtering has various filters based on Canny and Sobel operators. Low and high pass filtering algorithms often contradict each other, so it is often necessary to reduce noise by low pass filtering before edge detection and adjust the parameters to deal with more image noise without losing high-frequency edges [39].

The ideal low pass filter model can be expressed as follows:

$$H(x, y) = \begin{cases} 1, D(x, y) \leq D_0 \\ 0, D(x, y) \geq D_0 \end{cases}, \tag{3}$$

where D_0 is the passband radius, and $D(x, y)$ is the distance to the center of the spectrum, also known as the Euclidean distance; it can be calculated as follows: $D(x, y) = \sqrt{(x - X/2)^2 + (y - Y/2)^2}$, where X and Y denote the size of the spectrum image, and $(X/2, Y/2)$ denote the center of the spectrum.

The Gaussian low pass filter can be expressed as follows:

$$H(x, y) = e^{\frac{-D^2(x, y)}{2D_0^2}}. \tag{4}$$

After obtaining the low pass filter expression, the high pass filter expression can be construct by subtracting the low pass filter model by 1.

For better noise removal, the response function $H(j\omega)$ needs to be continuously adjusted. Therefore, the convolution function $G(j\omega)$ needs to be found to further improve the input signal $X(j\omega)$ according to the output:

$$\hat{X}(j\omega) = G(j\omega) * Y(j\omega). \tag{5}$$

The filter function in the frequency field can be expressed as follows:

$$G(f) = \frac{H^*(f)R(f)}{|H(f)|^2 R(f) + N(f)} = \frac{H^*(f)}{|H(f)|^2 + N(f)/R(f)}, \tag{6}$$

where $G(f)$ and $H(f)$ denote the Fourier transform of $h(t)$ and $g(t)$ in the frequency field, and $R(f)$ and $N(f)$ denote the power spectrum of the input function $x(t)$ and additive noise $n(t)$ in the frequency field, respectively. * denotes the
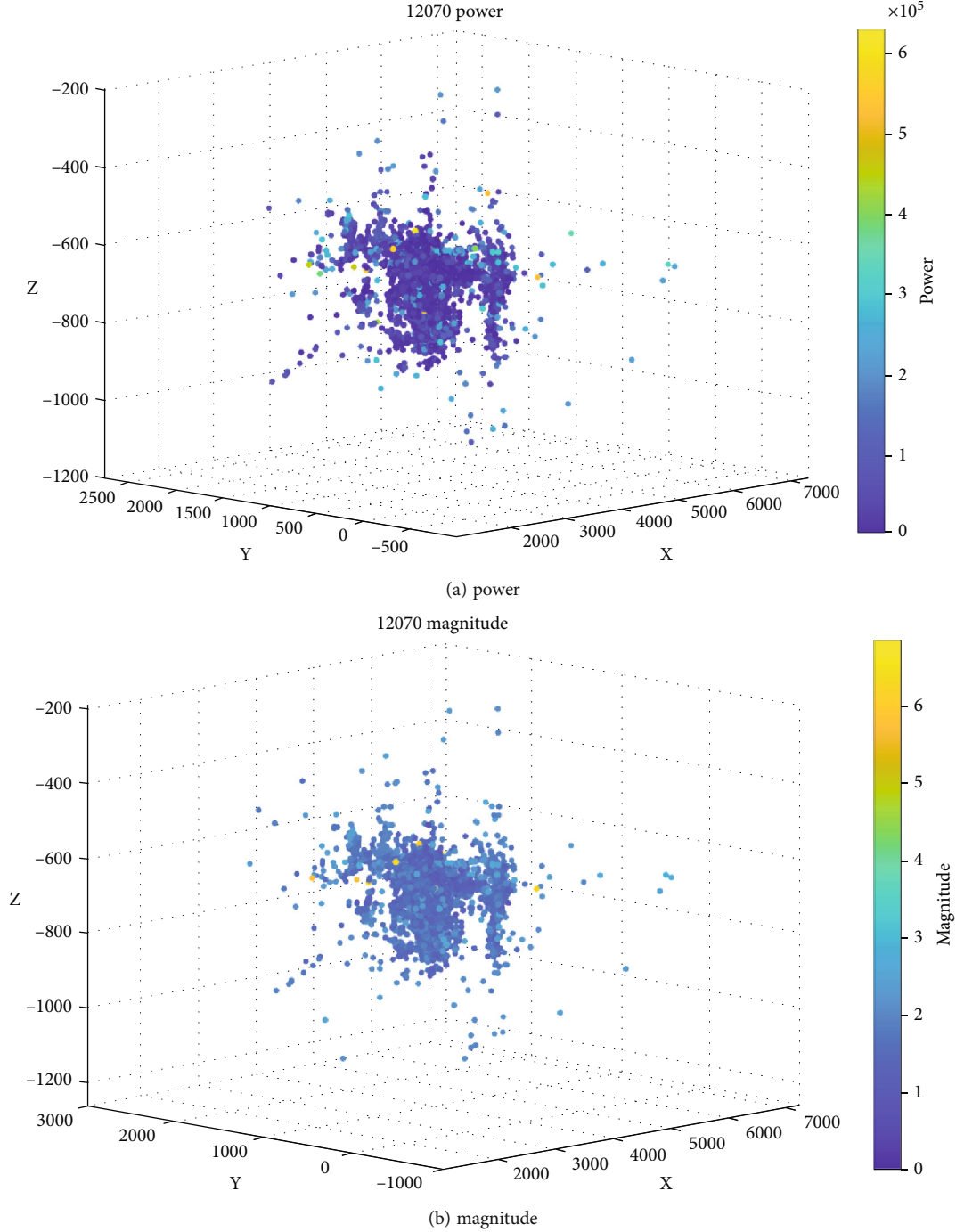
(a) power

(b) magnitude

Figure 2: Energy and magnitude of 12070 working face coal seam.

conjugate complex number. Equation (6) can be further rewritten as follows:

$$G(f) = \frac{1}{H(f)} \left[\frac{|H(f)|^2}{|H(f)|^2 + N(f)/R(f)} \right]. \tag{7}$$

where $N(f)/R(f)$ denotes the signal-to-noise ratio. When the signal-to-noise ratio tends to infinity, i.e., the noise closes to zero, the above equation is equal to 1, so the filtering is simpli-

fied as an inverse filtering process. However, when the noise increases, the signal-to-noise ratio decreases, and the values of the above parameters decrease as well. This suggested that the bandpass frequency of the filtering depends on the signal-to-noise ratio. Substituting Equation (7) into Equation (5), the input signal $\widehat{X}(f)$ in the frequency field can be obtained:

$$\widehat{X}(f) = \frac{1}{H(f)} \left[\frac{|H(f)|^2}{|H(f)|^2 + N(f)/R(f)} \right] * Y(f). \tag{8}$$
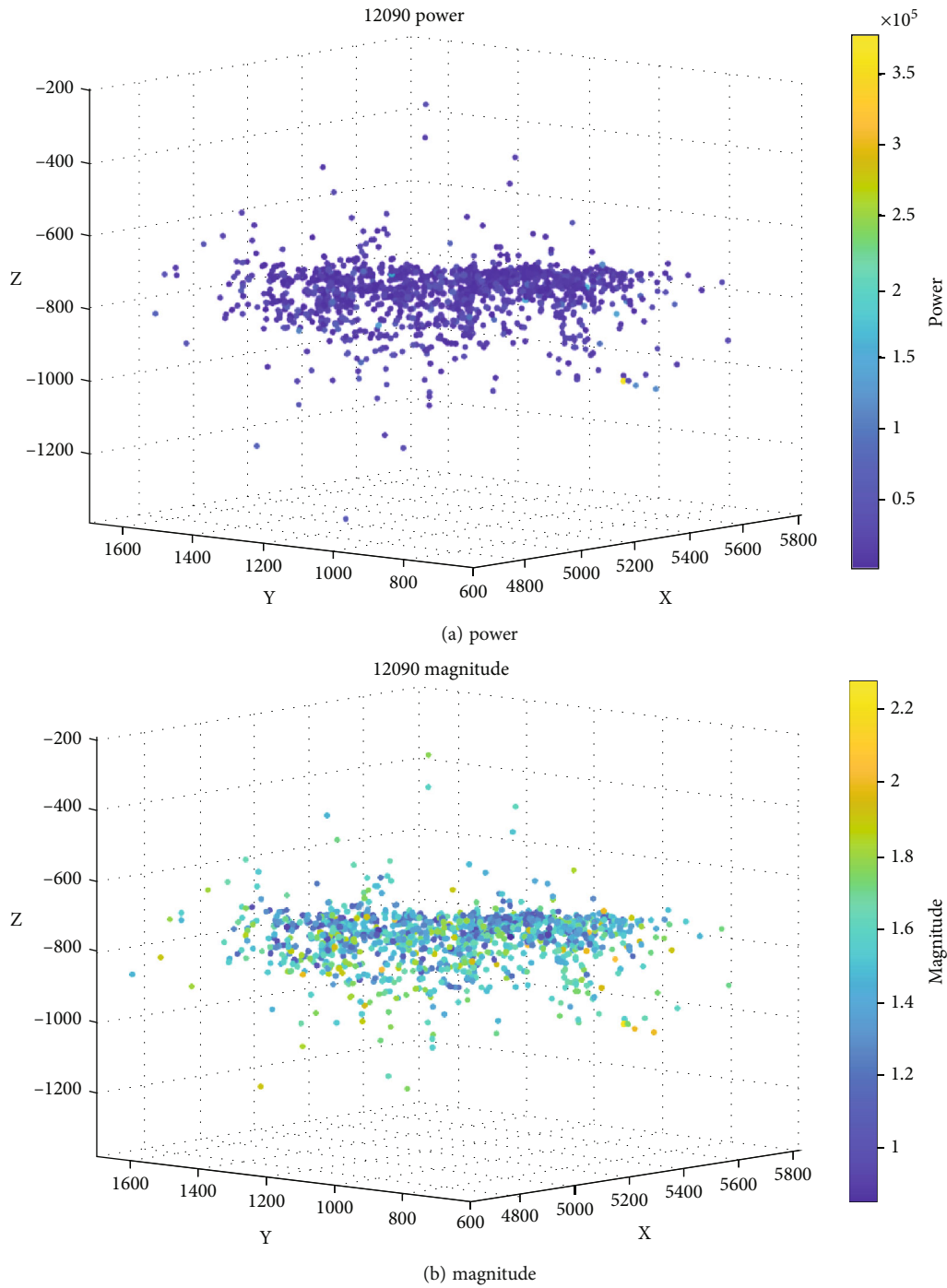
(a) power

(b) magnitude

FIGURE 3: Energy and magnitude of 12090 working face coal seam.

After obtaining $\hat{X}(f)$, the deconvolution result $\hat{x}(f)$ can be obtained by the inverse Fourier variation.

The original microseismic waveform obtained from the sensor was filtered, and the microseismic energy and magnitude data obtained were shown in Figures 2 and 3. The filtered data will be used to build a prediction model by GP for the energy and magnitude data in next section.

4. Energy and Magnitude Prediction Modeling

GP, as an improvement of GA [40], has been widely used in geotechnical engineering for reservoir mechanics prediction and simulation [41–43]. The principle is based on the survival of the fittest of the genetic law, which simulates the reproduction and evolution of populations (e.g., replication, crossover, and mutation) to generate optimal individuals for

TABLE 2: Parameters of the GP model.

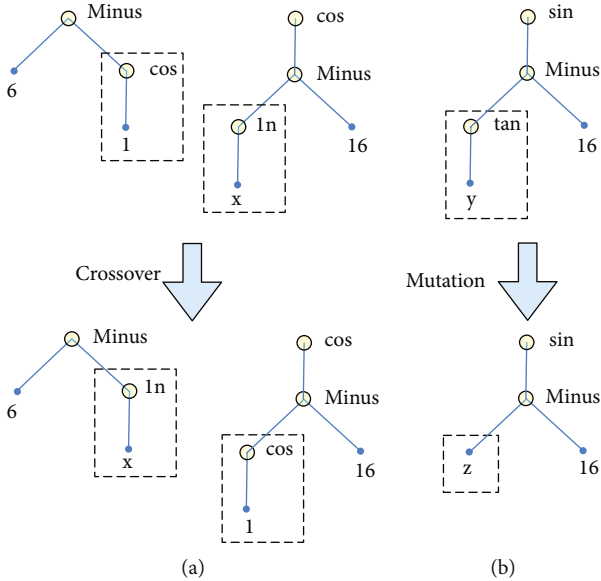| GP parameter	Values
Terminal set	x, y, z
Function set	+, -, ×,/, sin, cos, tan, exp, sqrt, ln, power
Prediction set	Power and magnitude
Fitness function	Sum_{er}
Maximum generation	100
Population size	100
Tree initialization	Ramped half-and-half
Selection method	Tournament
Genetic operators	Mutation, crossover, replication
Mutation rate	Dynamic (initial value 0.5)
Crossover rate	Dynamic (initial value 0.5)
Reproduction rate	Dynamic (initial value 0)
Termination criterion	Maximum generation

FIGURE 5: Evolution of operator probabilities and cumulative occurrences.

FIGURE 4: Schematic diagram of individual (a) crossover and (b) mutation.
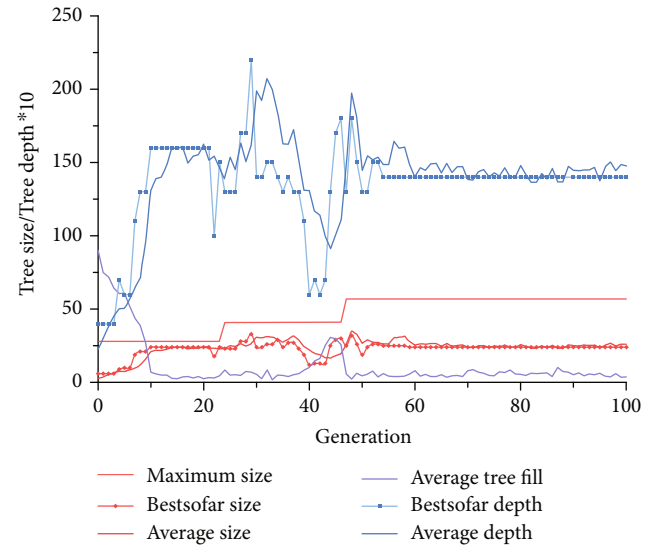
FIGURE 6: Evolution of tree size and depth in population.

given condition. In contrast to GA, GP utilizes tree structure codes to represent individuals in a population instead of binary code lines of GA [35, 44]. The tree structure individuals consist of predictor variables, mathematical symbols, and numbers, and the expressions of output variables can be constructed under fixed output rules. Genetic operators (replication, crossover and mutation, etc.) are used on tree-structured individuals in population to create new offspring programs. It can generate the best individual, also known as the individual with the highest fitness, i.e., the equation with the best prediction, under the rule of the survival of the fittest [45]. The sum of the absolute error between the measured and predicted values of an individual (Sum_{er}) is used as a measure of fitness in GP. This means that a lower Sum_{er} corresponds
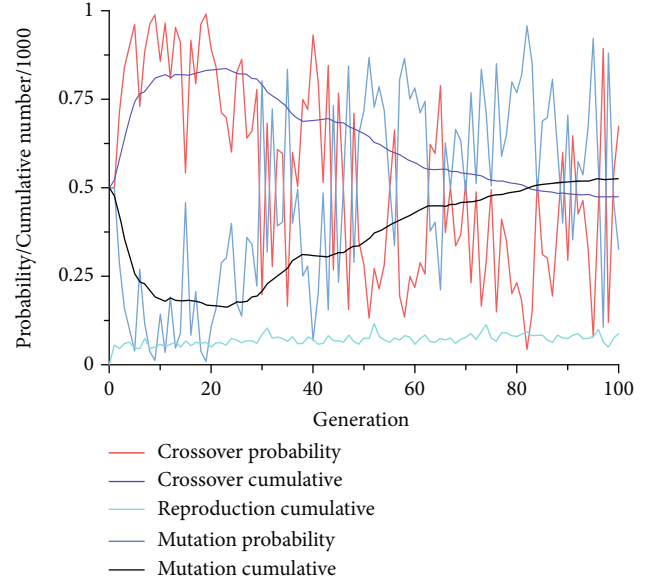
to a higher fitness, and the Sum_{er} equation can be expressed as follows:

$$Sum_{er} = \sum_{i=1}^{N} \left| ms_{mi} - ms_{pi} \right|, \tag{9}$$

where ms_{mi} is the microseismic data obtained through the field; ms_{pi} is the microseismic data predicted by GP. N is the overall number of samples.

Table 2 shows the parameters used in the GP modeling. In this study, the three-dimensional coordinates (x, y, and z) of the subsurface space were used as predictor variables, and the energy and magnitude data were used as output variables
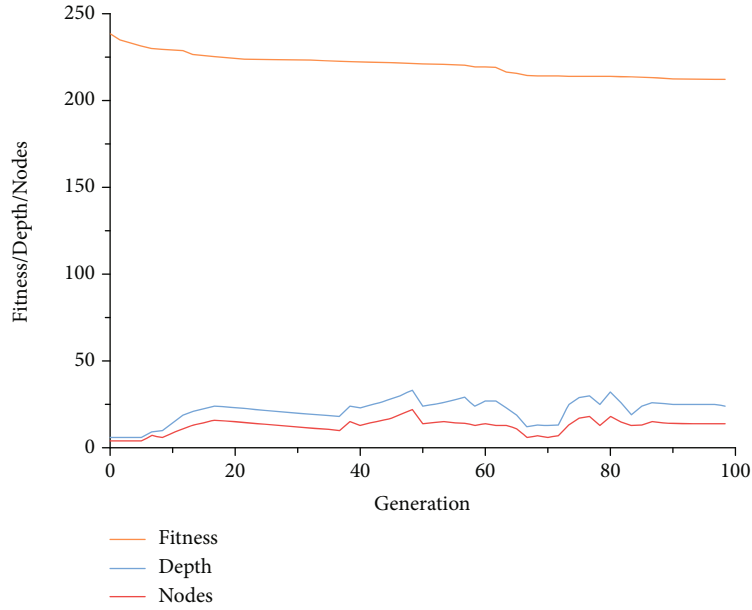
FIGURE 7: Fitness, depth, and nodes evolution of the optimal individual.

to be predicted using the coordinates. In the initialization of the microseismic population, the ramped half-and-half method was used to generate microseismic individuals with different breadth and dimensions to enhance diversity [36]. In the selection of microseismic individuals, the tournament method was used to randomly select a certain number of highly adapted individuals from the microseismic population as parents using high fitness as the criterion, and then create offspring of microseismic individuals using genetic operators including replication, crossover, and mutation [36]. The highest fitness individuals in each generation are directly entered into the offspring by the replication operator, and the number of replications can be specified by the user. For the remaining positions of next generation individuals, the microseismic individuals are genetically manipulated according to the programmed crossover and mutation probabilities.

Subtree crossover is the selection of random crossover points (nodes) of microseismic parents and replacement to create new microseismic individuals, and the crossover is shown in Figure 4(a). Mutation is the selection of a random mutation node of a microseismic individual and replacing the subtree of that node using the system randomly generated microseismic individuals, and the mutation is shown in Figure 4(b). The initial values of crossover and mutation probabilities are the default values in the system settings. The initial values of mutation and crossover probabilities are set to 0.5, and they are adjusted at any time during the population iteration to reflect the operator performance. An increase in the operator probability indicates that the produced microseismic individuals are more adaptive than the previous generation; at the same time, it decreases the probability of producing individuals that are poorly adapted to the environment. The microseismic individuals with the highest fitness obtained during the final run of the algorithm are the predicted results of GP.
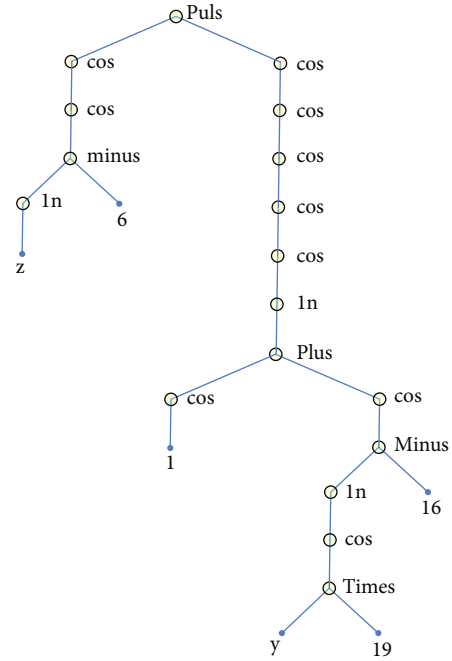

FIGURE 8: Optimal tree expression generated by GP.

The energy and magnitude data are substituted into the GP separately, and the following prediction curves can be obtained. The functions of the algorithm running of population iteration can be presented separately, taking the magnitude prediction of working face 12090 as an example. Figure 5 shows the dynamic evolution of the crossover and mutation probabilities during the algorithm run, and the cumulative occurrence of crossover, mutation, and replication operators. When the individuals with high fitness of population appeared, the replication operator would be introduced to replicate the high fitness individuals directly

Table 3: Prediction parameters of rock strength obtained by GP.

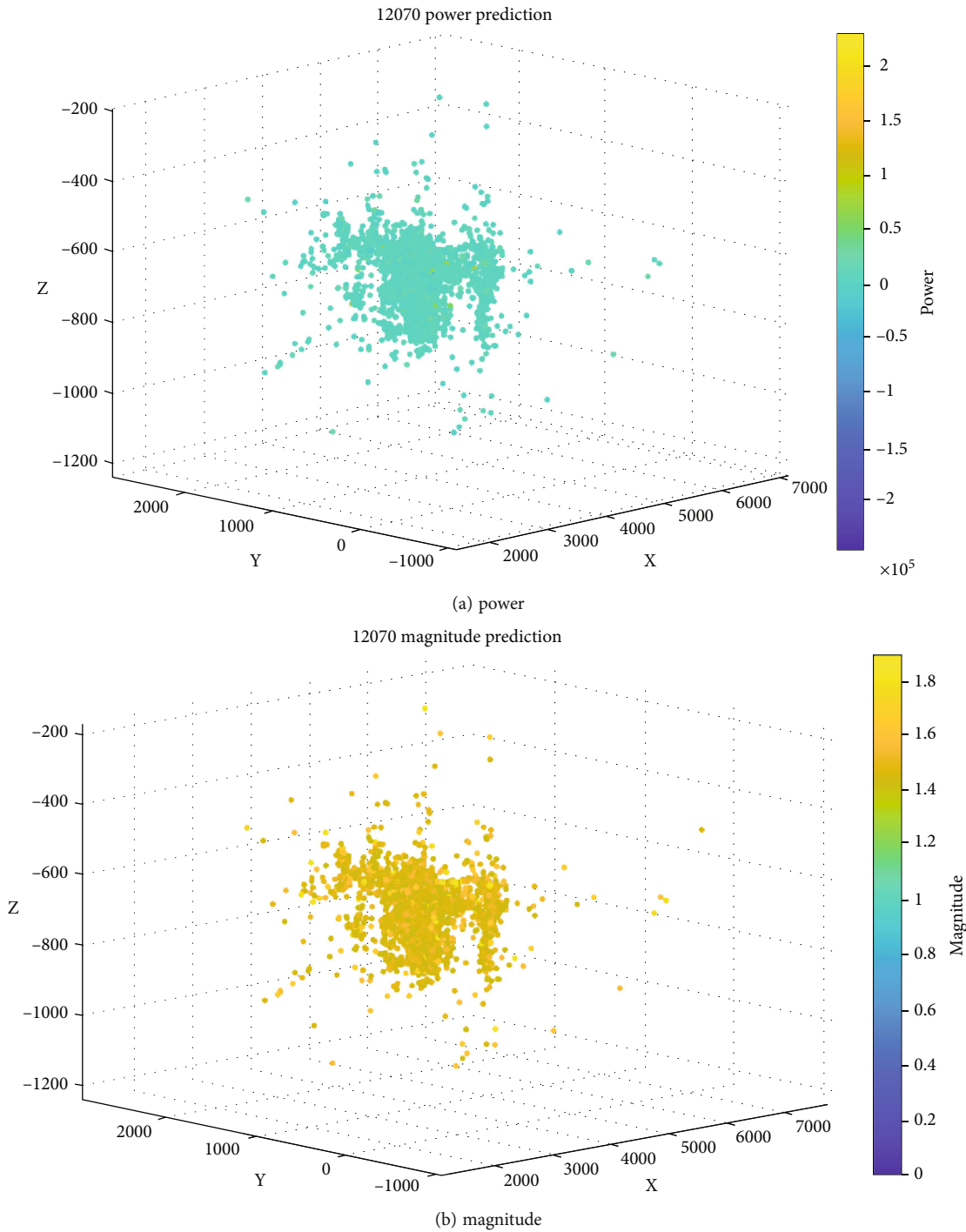| Modeling object	Depth	Nodes	Generation	Fitness	R^2	Equation
12070 power	12	61	100	1.97e8	0.56	$\text{power} = 10.97 - \left(\begin{array}{c} Y + 30Z + 21062.42 + \sin{(204Y - 137059)} \\ +\ln{(\cos{(6 + \ln{Y})}) \cdot (15Y - 35.10)} \end{array} \right)$
12070 magnitude	8	19	80	1665.83	0.74	$\text{magnitude} = \cos{(\cos{(\ln{(43 + Z + 0.80394Y)})})} + 0.89$
12090 power	26	53	100	1.42e7	0.78	$\text{power} = 27 \times (30 \times (\ln{(24 \times (\ln{(116 - 24 \times \varepsilon)} - 37)} - Z) - 12)} - (Z + 30))$ $\varepsilon = (24 \times (\ln{(52 - 24 \times (\ln{(-27 - Z)} - 37)}) - 37)} - Z - 27)$
12090 magnitude	14	24	100	212.32	0.88	$\text{magnitude} = \cos{(\cos{(\cos{(\cos{(\cos{(\ln{(\cos{1} + \cos{(\ln{(\cos{(\ln{(19Y)}} - 6)}}))})))))} + \cos{(\cos{(\ln{Z} - 6)})}$

(a) power

(b) magnitude

FIGURE 9: Prediction of power and magnitude of 12070 working face coal seam.

to the next generation to increase the average fitness of the population, and the occurrence of the replication operator in the last generation is 87. It can be found from the figure that the crossover operator has a higher ability than the mutation operator to produce highly adapted individuals in the early iterations of the population. However, as the population evolves, the fitness stabilizes, and the mutation ability of the magnitude individuals needs to be improved

to create better individuals. The ability of mutation operator to create the best individuals was higher than that of crossover in the late evolutionary stage, with 474 and 525 occurrences of crossover and mutation operators in the last generation, respectively.

Figure 6 shows the maximum, optimum, and average sizes and depths of the population individuals in the 12090-magnitude modeling. As the population multiplies, the size
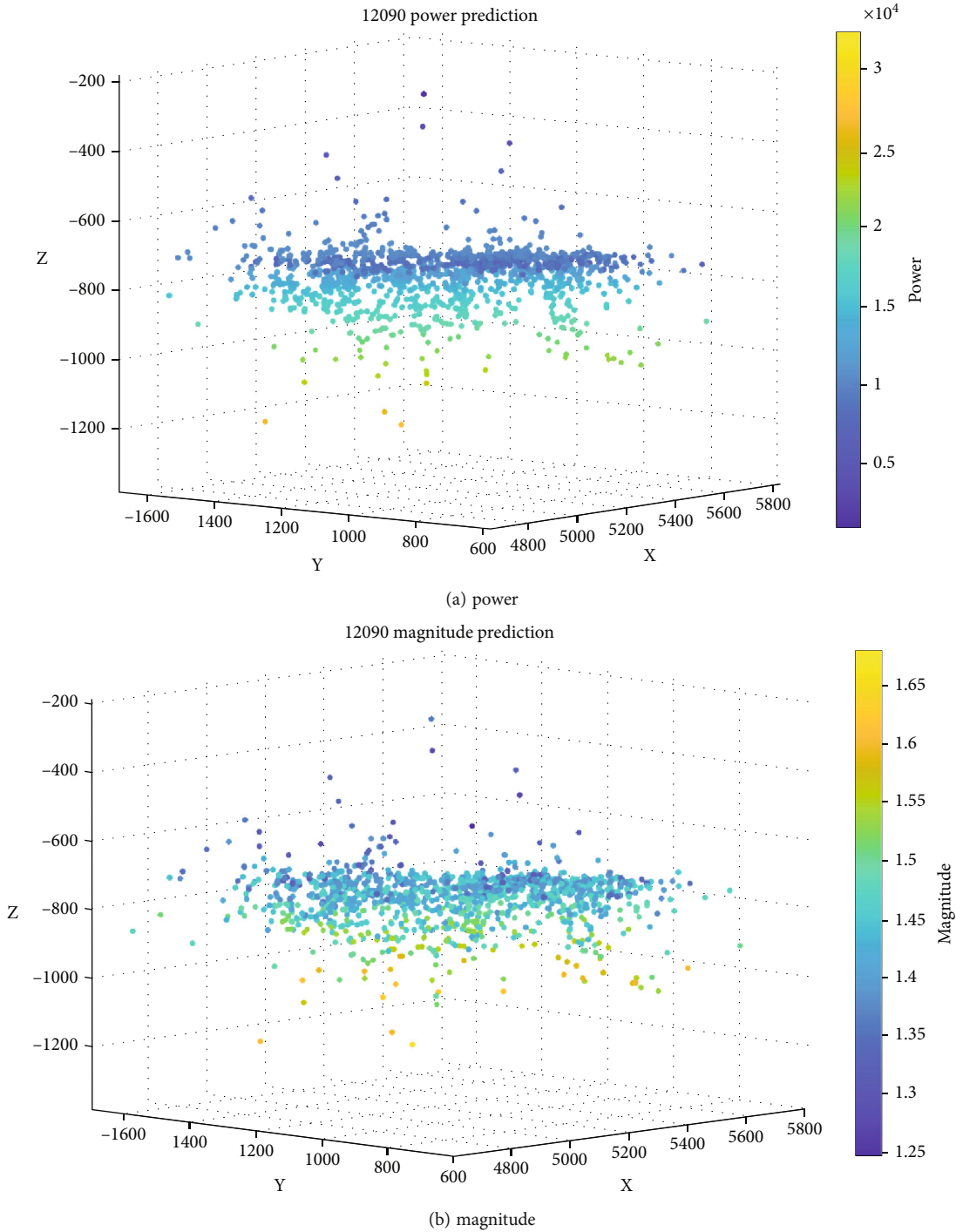
(a) power

(b) magnitude

FIGURE 10: Prediction of power and magnitude of 12090 working face coal seam.

and depth of the population individuals increase. The magnitude prediction expressions, represented by the magnitude individuals, also gradually increase in complexity but also gradually stabilize as the generation increases. The purple curve in the figure represents the average fill rate of population individuals, which is closely related to population diversity. The average filling rate represents the filling degree of each individual, and the average filling rate of unevenly developed individuals is low. At the beginning of the program, the average fill rate presents a sudden decrease, but the decrease gradually tends to be balanced. The lower average fill rate implies higher population diversity, which shows uneven development of individuals. This phenomenon is related to the ramped half-and-half method invoked to generate microseismic individuals with different breadth and dimensionality. Figure 7 shows the

fitness, number of nodes, and depth evolution of the optimal individuals in each generation. Since we used the sum of absolute error (Sum_{er}) between the measured and predicted values of individuals as a measurement of fitness, it can be found that the fitness of the optimal individuals gradually increases, showing a continuous decrease in Sum_{er}. The best individual appeared at 90th generation of population evolution, and the fitness of the best individual was 212.20, the depth of the tree was 14, and the number of nodes was 24.

The tree expression of the magnitude individual with the highest fitness generated at the end of the population iteration for a given 3D coordinate environment is shown in Figure 8. To obtain the prediction formula for the magnitude, we traversed each node starting from the bottom and left node, based on the rule of bottom to top and left to right, until the top of the tree. The final generated prediction formulas are shown in Table 3. Table 3 shows the depth, number of nodes, iterative generations, fitness (Sum_{er}), R^2, and the final prediction formula for the energy and magnitude optimal individuals of 12070 and 12090 working faces. From the equations, the coordinates y and z have a greater influence on energy and magnitude and show a significant role in the prediction. In contrast, the x-direction does not show a significant difference between energy and magnitude, so the x-coordinate does not appear in the prediction formula for magnitude and energy. Substituting the coordinates into the prediction formula, the obtained energy and magnitude data for the two working surfaces are shown in Figures 9 and 10. Due to the excavation and unloading effect on the working face, the mining stress causes the high energy and magnitude at the edge of the working face, and the energy and magnitude evolution predicted by GP can also describe this phenomenon well. Comparing Figure 3, Figure 4, and Figure 9 with Figure 10, it can be found that the actual magnitude and energy data of the working face fit well with the predicted data, and R^2 does not show an accurate fit due to the large amount of data obtained, but it is within the acceptable range. This implied that GP shows good performance in predicting the energy and magnitude signals in the field.

5. Conclusion

In this study, we established the magnitude and energy prediction formulas by GP and obtained the real-time evolution of each parameter of the optimal individual based on a large amount of energy and magnitude data from the 12070 and 12090 working faces of Shoushan Mine of Pingdingshan Coal Group in China. The data were filtered, and a prediction model of microseismic data was constructed based on underground spatial three-dimensional coordinates. The main conclusions of this study are as follows:

(i) Since the original microseismic waveform contains large background noise, the original waveform was filtered. The filter function was designed to convolve the function $G(j\omega)$ in the frequency field, and the input signal $X(j\omega)$ can be continuously improved according to the output, and $\hat{x}(f)$ after deconvolution can be obtained by the inverse Fourier variation, and then the noise elimination was achieved

(ii) The magnitude and energy prediction formulas are established by GP. The real-time evolution of each parameter of the optimal individual is obtained. The actual magnitude and energy data of the working face show good agreement with those predicted by the GP prediction formulas. Due to the excavation and unloading effect of working face, the mining stress causes the high energy and magnitude at the edge of the surface, and the energy and magnitude evolution predicted by GP can also show this phenomenon well

Data Availability

The experimental data supporting the conclusions are available from the corresponding author on request.

Conflicts of Interest

The authors declare that they have no known competing financial interests or personal relationships that could have appeared to influence the work reported in this paper.

Acknowledgments

References

[1] X. Guo, X. Cai, J. Liu et al., "Natural gas exploration progress of sinopec during the 13th five-year plan and prospect forecast during the 14th five-year plan," *Nat. Gas Ind. B.*, vol. 9, no. 2, pp. 107–118, 2022.

[2] H. Xie, L. Wu, and D. Zheng, "Prediction on the energy consumption and coal demand of China in 2025," *Journal of China Coal Society*, vol. 44, no. 7, pp. 1949–1960, 2019.

[3] Y. Xue, J. Liu, P. G. Ranjith, F. Gao, H. Xie, and J. Wang, "Changes in microstructure and mechanical properties of low-permeability coal induced by pulsating nitrogen fatigue fracturing tests," *Rock Mechanics and Rock Engineering*, 2022.

[4] G. Yin, M. Li, J. G. Wang, J. Xu, and W. Li, "Mechanical behavior and permeability evolution of gas infiltrated coals during protective layer mining," *International Journal of Rock Mechanics and Mining Sciences*, vol. 80, pp. 292–301, 2015.

[5] W. J. Gale, "A review of energy associated with coal bursts," *International Journal of Mining Science and Technology*, vol. 28, no. 5, pp. 755–761, 2018.

[6] J. Lu, G. Yin, H. Gao et al., "True triaxial experimental study of disturbed compound dynamic disaster in deep underground coal mine," *Rock Mechanics and Rock Engineering*, vol. 53, no. 5, pp. 2347–2364, 2020.

[7] B. Shen, Y. Duan, X. Luo et al., "Monitoring and modelling stress state near major geological structures in an underground coal mine for coal burst assessment," *International Journal of Rock Mechanics and Mining Sciences*, vol. 129, p. 104294, 2020.

[8] Y. Xue, P. G. Ranjith, Y. Chen, C. Cai, F. Gao, and X. Liu, "Nonlinear mechanical characteristics and damage constitutive model of coal under CO_2 adsorption during geological sequestration," *Fuel*, vol. 331, p. 125690, 2023.

[9] B. Zhou, J. Xu, S. Peng et al., "Effects of geo-stress on the dynamic response of multi-physical field parameters during coal and gas outbursts under true triaxial stress," *International Journal of Rock Mechanics and Mining Sciences*, vol. 142, p. 104759, 2021.

[10] L. Liu, W. Song, C. Zeng, and X. Yang, "Microseismic event detection and classification based on convolutional neural network," *Journal of Applied Geophysics*, vol. 192, no. 6, p. 104380, 2021.

[11] Y. Wang, Q. Qiu, Z. Lan et al., "Identifying microseismic events using a dual-channel CNN with wavelet packets decomposition coefficients," *Comput. Geosci-UK.*, vol. 166, p. 105164, 2022.

[12] C. Zhang, G. Jin, C. Liu et al., "Prediction of rockbursts in a typical island working face of a coal mine through microseismic monitoring technology," *Tunn. Undergr. Sp. Tech.*, vol. 113, p. 103972, 2021.

[13] H. Gao, M. Zhang, N. Hou, and H. Dong, "Dynamic-transmission-based recursive filtering algorithm for microseismic event detection under sensor saturations," *Measurement*, vol. 186, p. 110197, 2021.

[14] F. Liu, C. Tang, Y. Zhang, and T. Ma, "Rockburst and microseismicity characteristics in the qinling water conveyance tunnel of the hanjiang-to-weihe river diversion project," *International Journal of Rock Mechanics and Mining Sciences*, vol. 148, p. 104973, 2021.

[15] W. Cao, S. Durucan, W. Cai, J.-Q. Shi, and A. Korre, "A physics-based probabilistic forecasting methodology for hazardous microseismicity associated with longwall coal mining," *International Journal of Coal Geology*, vol. 232, p. 103627, 2020.

[16] C. Ma, T. Li, H. Zhang, Y. Jiang, and T. Song, "A method for numerical simulation based on microseismic information and the interpretation of hard rock fracture," *Journal of Applied Geophysics*, vol. 164, pp. 214–224, 2019.

[17] R. Xue, Z. Liang, N. Xu, and L. Dong, "Rockburst prediction and stability analysis of the access tunnel in the main powerhouse of a hydropower station based on microseismic monitoring," *International Journal of Rock Mechanics and Mining Sciences*, vol. 126, p. 104174, 2020.

[18] L. Tang, C. Yang, and C. Pan, "Optimization of microseismic monitoring network for large-scale deep well mining," *Chinese Journal of Rock Mechanics and Engineering*, vol. 10, pp. 2036–2042, 2006.

[19] S. C. Maxwell, J. Rutledge, R. Jones, and M. Fehler, "Petroleum reservoir characterization using downhole microseismic monitoring," *Geophysics*, vol. 75, no. 5, pp. 75A129–75A137, 2010.

[20] C. Tang, J. Wang, and J. Zhang, "Preliminary engineering application of microseismic monitoring technique to rockburst prediction in tunneling of jinping II project," *Journal of Rock Mechanics and Geotechnical Engineering*, vol. 2, no. 3, pp. 193–208, 2010.

[21] X. Zhang, W. Zhang, and J. Zhang, "Detecting and locating microseismic events with stacking velocity analysis for surface monitoring," *Journal of Applied Geophysics*, vol. 195, p. 104470, 2021.

[22] L. Qiu, Z. Liu, E. Wang, and B. Li, "Early-warning of rock burst in coal mine by low-frequency electromagnetic radiation," *Engineering Geology*, vol. 279, p. 105755, 2020.

[23] H. Lv, "Noise suppression of microseismic data based on a fast singular value decomposition algorithm," *Journal of Applied Geophysics*, vol. 170, p. 103831, 2019.

[24] Y. Xin, B. Qla, H. C. Xing, and B. Ypa, "Real-time prediction of rockburst intensity using an integrated cnn-Adam-Bo algorithm based on microseismic data and its engineering application," *Tunn. Undergr. Sp. Tech.*, vol. 117, p. 104133, 2021.

[25] S. Xu, C. Zhang, Z. Chen, Y. Li, and J. Liu, "Accurate identification of microseismic waveforms based on an improved neural network model," *Journal of Applied Geophysics*, vol. 190, p. 104343, 2021.

[26] J. X. Wang, S. B. Tang, M. J. Heap, C. A. Tang, and L. X. Tang, "An auto-detection network to provide an automated real-time early warning of rock engineering hazards using microseismic monitoring," *International Journal of Rock Mechanics and Mining Sciences*, vol. 140, no. 21, article ???, 2021.

[27] S. Tang, J. Wang, and C. Tang, "Identification of microseismic events in rock engineering by a convolutional neural network combined with an attention mechanism," *Rock Mechanics and Rock Engineering*, vol. 54, no. 1, pp. 47–69, 2021.

[28] K. Ma, X. Y. Sun, C. A. Tang, F. Z. Yuan, S. J. Wang, and T. Chen, "Floor water inrush analysis based on mechanical failure characters and microseismic monitoring," *Tunn. Undergr. Sp. Tech.*, vol. 103698, 2021.

[29] A. Mottahedi and M. Ataei, "Fuzzy fault tree analysis for coal burst occurrence probability in underground coal mining," *Tunn. Undergr. Sp. Tech.*, vol. 83, pp. 165–174, 2019.

[30] D. Wamriew, M. Charara, and D. Pissarenko, "Joint event location and velocity model update in real-time for downhole microseismic monitoring: a deep learning approach," *Comput. Geosci-UK.*, vol. 158, p. 104965, 2022.

[31] M. Gandomi, A. R. Kashani, A. Farhadi, M. Akhani, and A. H. Gandomi, "Spectral acceleration prediction using genetic programming based approaches," *Applied Soft Computing*, vol. 106, p. 107326, 2021.

[32] L. Vanneschi and M. Castelli, "Soft target and functional complexity reduction: a hybrid regularization method for genetic programming," *Expert Systems with Applications*, vol. 177, p. 114929, 2021.

[33] C. Wang, G. W. Ma, J. Zhao, and C. K. Soh, "Identification of dynamic rock properties using a genetic algorithm," *International Journal of Rock Mechanics and Mining Sciences*, vol. 41, pp. 490–495, 2004.

[34] M. Fener, S. Kahraman, A. Bilgil, and O. Gunaydin, "A comparative evaluation of indirect methods to estimate the compressive strength of rocks," *Rock Mechanics and Rock Engineering*, vol. 38, no. 4, pp. 329–343, 2005.

[35] M. K. Salooki, M. Esfandyari, E. Rabbani, M. Koulivand, and A. Azarmehr, "Application of genetic programing technique for predicting uniaxial compressive strength using reservoir formation properties," *Journal of Petroleum Science and Engineering*, vol. 159, pp. 35–48, 2017.

[36] B. Yu, H. Zhao, J. Tian et al., "Modeling study of sandstone permeability under true triaxial stress based on backpropagation neural network, genetic programming, and multiple regression analysis," *Journal of Natural Gas Science and Engineering*, vol. 103742, 2021.

[37] M. R. Rezaei, K. Arai, L. M. Frank, U. T. Eden, and A. Yousefi, "Real-time point process filter for multidimensional decoding problems using mixture models," *Journal of Neuroscience Methods*, vol. 109006, 2021.

[38] Y. Wan, *MATLAB Implementation of Digital Signal Processing*, Science Press, 2012.

[39] J. Zhang, J. Hou, and Z. Zhang, "Real-time identification of out-of-control and instability in process parameter for gasification process: integrated application of control chart and Kalman filter," *Energy*, vol. 238, p. 121845, 2022.

[40] J. R. Koza, *Genetic Programming: On the Programming of Computers by Means of Natural Selection*, MIT Press, Cambridge, Mass, 1992.

[41] T. Kötzing, J. A. G. Lagodzinski, J. Lengler, and A. Melnichenko, "Destructiveness of lexicographic parsimony pressure and alleviation by a concatenation crossover in genetic programming," *Theoretical Computer Science*, vol. 816, pp. 96–113, 2020.

[42] S. Silva and E. Costa, "Dynamic limits for bloat control in genetic programming and a review of past and current bloat theories," *Genet. Program. Evol. M.*, vol. 10, no. 2, pp. 141–179, 2009.

[43] Q. L. Wu, P. H. Cournede, and A. Mathieu, "An efficient computational method for global sensitivity analysis and its application to tree growth modelling," *Reliability Engineering and System Safety*, vol. 107, no. 1, pp. 35–43, 2012.

[44] S. Q. Ni, C. J. Tang, N. Yang, and J. Zuo, "Gene expression programming algorithm based on multi-threading evaluator," *J. Comput. Appl.*, vol. 32, no. 4, pp. 986–989, 2012.

[45] A. Majdi and M. Beiki, "Evolving neural network using a genetic algorithm for predicting the deformation modulus of rock masses," *International Journal of Rock Mechanics and Mining Sciences*, vol. 47, no. 2, pp. 246–253, 2010.